



Transverse compression failure of unidirectional composites

Y. Hu*, N.K. Kar and S.R. Nutt

Gill Composites Center, Department of Chemical Engineering and Materials Science,
University of Southern California, Los Angeles, California

Abstract:

The mechanical response of unidirectional composites subject to uniaxial transverse compressive loads was measured and analyzed by finite element simulation. Consistency in failure plane orientation was observed when comparing simulated matrix shear band angle to measured crack angle. A model based on hexagonal packing of fibers was proposed and the shear band angle was shown to depend on the fiber volume fraction. The effects of strong and weak fiber–matrix interfaces were considered using models with randomly distributed fibers for a valid statistical analysis. The results of these models showed that the composite compressive strength increased with the fiber loading for the strong interface case, while the strength was independent of the fiber loading for the weak interface case because of interface debonding. *POLYM. COMPOS.*, 36:756–766, 2015. ©

2014 Society of Plastics Engineers

Key words: A-Short-Fibre Composites, C-Finite Element Analysis (FEA), C-Modelling, Mean-field homogenization

1. Introduction

Unidirectional (UD) composites generally exhibit high stiffness and tensile strength in the longitudinal direction, although these same properties are much lower in the transverse directions.

The overall compressive failure of UD composites in many cases initiates from transverse cracking

Membrane-type metamaterials: Transmission loss of multi-celled arrays

Naify, Christina J. and Chang, Chia-Ming and McKnight, Geoffrey and Scheulen, Florian and Nutt, Steven, *Journal of Applied Physics*, 109, 104902 (2011), DOI:<http://dx.doi.org/10.1063/1.3583656>



[1]. The crack angle under uniaxial compression, which is the angle between the failure plane and the plane perpendicular to the loading axis, is generally 50° – 60° for UD composites with polymer matrix [2-6]. The neat polymer matrix also shows a failure plane angle greater than 50° [7-9] but is usually several degrees lower than the crack angles of composites. This difference stems from the presence of fibers and will be considered in this study.

Several theories address the failure of unidirectional composites [10-15] and attempt to describe the development of the failure plane. Mohr–Coulomb theory [10] assumes compressive failure occurs in the form of shear failure along a specific plane, and the orientation of the failure plane is determined by friction angle and cohesion, both intrinsic material properties. The failure plane angle range is 45° – 90° from Mohr–Coulomb theory. Christensen's theory [11] assumes the failure plane orientation is where the normal plastic strain increment is zero, and yields a failure plane angle range of 45° – 60° . Puck's theory [12] predicts that the failure plane occurs where the angle-dependent effort function reaches a maximum. The transverse failure plane angle and strength are affected not only by transverse properties but also by the longitudinal stress state. All the above theories generally treat composites as a continuum, and do not account for microscopic failure mechanisms involving fiber–matrix interactions, which is critical to understanding composite failure mechanisms.

Several recent simulation studies have attempted to address micro-level failure mechanisms [6, 16-22]. For example, LLorca and coworkers [6, 19, 20] investigated transverse properties of UD composites using the representative volume element (RVE) method by finite element simulation. Random distributions of fibers were simulated, and the influence of matrix and interface properties on the overall composite behavior was studied. In contrast, Blassiau et al. [16] studied the load transfer mechanism in UD composites using models with regularly packed fibers. The effect of fiber volume fraction and interface debonding on the load transfer and overall mechanical response was

“Transverse compression failure of unidirectional composites” Y. Hu, N. Kar, and S. Nutt, *Polymer Compos.* (2014) DOI<<http://dx.doi.org/2010.1002/pc.22996>>



investigated. Correa et al. [17, 18] studied the fiber–matrix interface crack growth in UD composites under transverse compression, using a single fiber model. Ghassemieh and Nassehi [21] investigated the influence of fiber loading on stress concentration, matrix failure, and interface debonding, and simulations were based on a model with hexagonally packed fibers. Kok and Meijer [22] studied the effect of fiber volume fraction, temperature, and interface adhesion on matrix yielding and fracture, using finite element models with quadratically and hexagonally packed fibers. However, simulations listed above did not address the issue of failure plane orientation, and the effect of fiber volume fraction was not studied using randomly distributed fibers. In any event, fiber distributions in composites are never regularly packed, and thus accurate simulations must feature statistically random spatial distributions of fibers.

Here, we use a micromechanics analysis to show how the fiber volume fraction (f) and interface strength influence failure plane angle, compressive strength, strain concentration, and interfacial debonding in UD composites loaded in transverse compression.

We build RVE models of different fiber volume fraction levels, and investigate the effect of fiber volume fraction on the failure plane orientation. The models were built with randomly distributed fibers. For each condition, a quantity of models with different fiber distributions was computed to obtain a statistically valid result. Simulation results show consistency with experimental data: failure plane angle increases with fiber volume fraction, depending on interface status. Experiments using samples with $f = 70\%$ were conducted, and finite element models of $f = 10\%$, 30% , and 50% were used. For comparison, experimental data of $f < 70\%$ from literature [2-6] were used. Simulation data for random RVE of $f > 50\%$ were not available because of numerical convergence difficulty.



2. Experiment

2.1 Specimen Preparation

Unidirectional glass fiber (E-glass 366) composite rod with an epoxy matrix (Lindoxy 190) was manufactured using a hot pultrusion process (Composite Technology Corporation, Irvine, CA), yielding rods with diameter of ~ 9 mm. The fiber volume fraction was $\sim 70\%$, measured by cutting and polishing a cross-section of the rod sample and viewing under scanning electron microscope (JEOL JSM-6610 SEM). The rod was further cut using a diamond saw (Struers Minitom) into cuboidal samples in the dimensions of height \times width \times thickness = $6 \times 3 \times 4$ mm³. The height-to-width ratio was 2:1 in accordance with conventional compression tests. Surfaces of the cuboidal samples were then polished to ensure that they were smooth and flat, and to ensure that the sample was in strict cuboidal shape to prevent rotation and shear during compression test. Finally, a black-and-white speckle pattern was applied to the front surface for accurate strain measurement by digital image correlation (DIC), as shown in Fig. 1.



Figure 1. Digital image correlation pattern of cuboidal sample.

2.2 Quasi- Static Compression Test

Cuboidal samples were transversely loaded in compression until fracture occurred using an electric-motor driven load frame (Instron 5567). The loading rate was low (1 mm/min) to ensure a quasi-static stress state in the sample and to minimize the strain rate effect. Sixteen samples in total were prepared and tested. During testing, load was recorded, and images of the DIC pattern on the front surface were recorded at selected time intervals. The images were post-processed using DIC analysis software (VIC-2D, Correlated Solution) to obtain accurate strain values. Crack angles were also measured from microscopic images after test, and fractography was performed using SEM (JEOL JSM-6610 SEM).

“Transverse compression failure of unidirectional composites” Y. Hu, N. Kar, and S. Nutt, *Polymer Compos.* (2014) DOI<<http://dx.doi.org/2010.1002/pc.22996>>



3. Finite Element Analysis

3.1 Model Generation

Micro-level 2D RVE models with randomly distributed fibers were generated using a code developed by the authors (Matlab, MathWorks), and static transverse compression was simulated using commercial software (Abaqus, Dassault Systemes). First, a sequential random algorithm [23] was used in the code to generate randomly distributed parallel fibers. In this algorithm, individual fibers are generated sequentially at random locations, and if a newly generated fiber overlaps with an existing one, it is re-generated until there is no overlap. Compared to the Monte Carlo algorithm, the sequential algorithm is simpler and faster, although the greatest f is generally limited to $<60\%$. Second, geometric information of the fibers such as center location and diameter was passed into a Python script. The script can be executed in Abaqus to generate the parts and assembly of fibers and matrix. The final step is defining material properties, interface and contact parameters, meshing the model, and running the analysis in Abaqus.

Three fiber volume fraction levels (10%, 30%, and 50%) were simulated. For each fiber volume fraction level, 10 iterations of models with different random fiber distributions were generated and computed for a statistical analysis. For each iteration, simulations were performed twice with the interface strength set to strong and weak, respectively, to study the influence of the interface on the overall mechanical response. Figure 2 shows one $f=50\%$ model with an inset to reveal the mesh detail. The model size was $(100 \times 100) \mu\text{m}$, and the fiber diameter was $10 \mu\text{m}$ with $0.5 \mu\text{m}$ standard deviation. Models with $f=10\%$ and 30% have the same model size and fiber dimension. The statistical distribution of fiber diameters was determined from SEM images of polished cross-

“Transverse compression failure of unidirectional composites” Y. Hu, N. Kar, and S. Nutt, *Polymer Compos.* (2014) DOI<<http://dx.doi.org/2010.1002/pc.22996>>



sections of the samples. For both fiber and matrix, the mesh size was 1 μm , and linear triangular plane strain elements (CPE3) were used. Interface nodes of fiber and matrix are allowed to overlap at the beginning of simulation to achieve interaction. Uniaxial transverse compression was simulated in the vertical direction using general static analysis step. The two side surfaces were constrained to be vertical and straight during compression, but no force or displacement boundary conditions were applied. We assumed a fiber modulus of 72.3 GPa and a Poisson's ratio of 0.22, values that are typical for E-glass fibers, and the fibers were assumed to be isotropic.

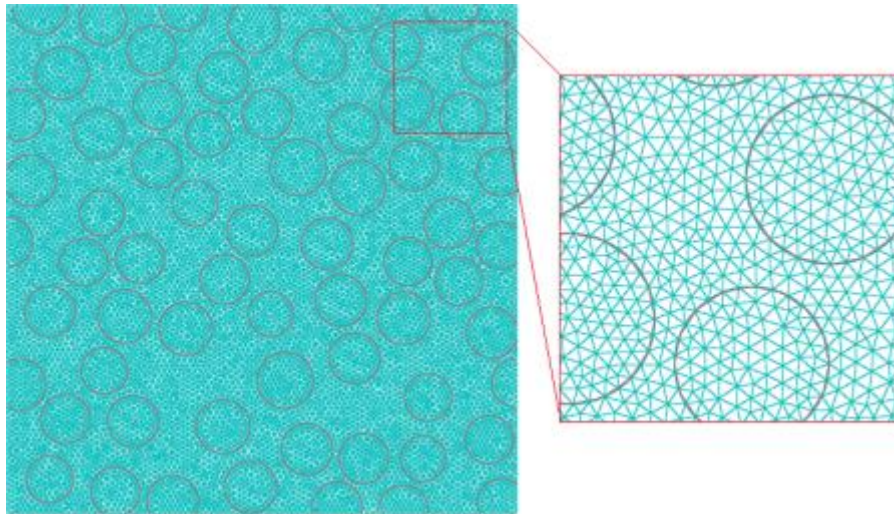


Figure 2. One $f = 50\%$ model mesh grid.

3.2 Matrix Failure Criterion and Progression rule

According to Mohr–Coulomb theory, failure under uniaxial compression occurs by shear failure along a specific plane. The shear strength (τ) on the failure plane is affected by the normal stress component (σ) on it. Equation (1) describes the Mohr–Coulomb failure criterion [24]:

$$\tau = c - \sigma \tan \phi, \quad (1)$$



in which c is the cohesion and ϕ is the friction angle, both of which are intrinsic properties of the material. The failure plane angle θ is given below (Eq. (2)):

$$\theta = \frac{1}{2} \left(\frac{\pi}{2} + \phi \right). \quad (2)$$

For epoxy, the measured failure plane angle is 50° – 60° [7-9], and the friction angle can be back-calculated from Eq. (2). A friction angle of 14° was used in the models, corresponding to a failure plane angle of 52° . The failure plane angle for a neat epoxy resin is reportedly 52° [7], although the mechanical properties for the polymer matrix in a composite can be quite different from that of the neat resin. Thus, this input value for the angle is chosen only for illustration purposes and for comparison with the failure plane angle of composites. A cohesion stress of 45 MPa was assumed, based on published data [7-9], and the compressive strength was calculated to be 115 MPa from Mohr–Coulomb theory. A modulus of 3.1 GPa was implemented and the matrix resin was assumed to be isotropic.

The failure progression rule (flow rule) from Ref. 25 was adopted, which describes material's behavior after the failure criterion (Eq. (1)) was reached. In this flow rule, the flow potential G for the yield surface is a hyperbolic function in the meridional stress plane (Eq. 3):

$$G = \sqrt{(\varepsilon c \tan \psi)^2 + (R_{mw} q)^2} - p \tan \psi, \quad (3)$$

where

$$R_{mw} = \frac{4(1-e^2)\cos^2\Theta + (2e-1)^2}{2(1-e^2)\cos\Theta + (2e-1)\sqrt{4(1-e^2)\cos^2\Theta + 5e^2 - 4e}} \cdot \frac{3 - \sin\phi}{6\cos\phi}$$



And $\cos(3\Theta) = \left(\frac{r}{q}\right)^3$

$$e = \frac{3 - \sin \phi}{3 + \sin \phi}$$

in which ε is the meridional eccentricity, ψ is the dilation angle, q is the Mises stress, p is the equivalent pressure stress, and r is the third invariant of deviatoric stress. A value of 0.1 was used for ε , which defines the rate at which the hyperbolic function approaches the asymptote. The dilation angle ψ , which defines the material volume expansion during shearing, is always less than or equal to the friction angle ϕ , and $\psi > 0$ indicates material expansion while $\psi < 0$ indicates contraction during shearing. When $\psi = \phi$, the plastic strain increment is always normal to the yield surface (i.e., associated flow), a condition that applies for metals but may not apply to polymers. A dilation angle of 12° was chosen for this study to simulate the general case of non-associated flow of polymers. A comparison was made between 12° and 14° dilation angles for the same model, and results were only slightly different, indicating that the final results are not sensitive to dilation angle. Both the failure criterion and progression rule of the matrix were implemented using the material definition module in Abaqus.

3.3 Fiber-Matrix Cohesive Interface

A cohesive interface [6, 19, 20] was used to describe the fiber–matrix debonding. Figure 3 shows the relationship between the interfacial stress (t) and the debonding displacement (δ).

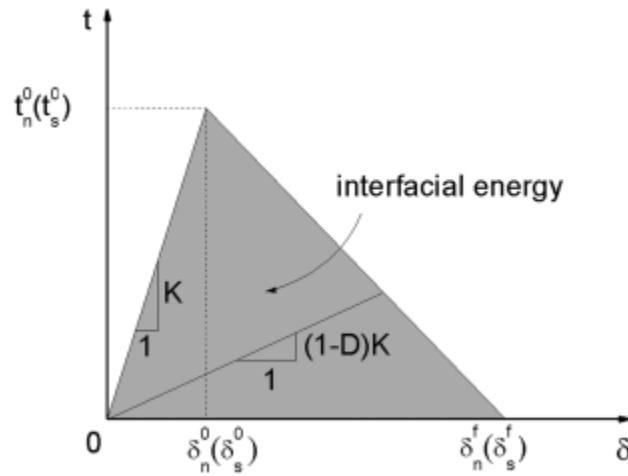


Figure 3. Interfacial debonding versus interfacial stress.

For a 2D problem, there are two interfacial stress components—normal (t_n) and shear (t_s), which are related to normal and shear separations δ_n and δ_s , respectively. There are two stages in the debonding process. In the first stage (initial loading), δ increases linearly with t (Eq. (4)), and no damage occurs. The second stage begins when t reaches a maximum (i.e., the debonding strength, t^0). From this moment, damage ensues, and t starts to decrease while δ starts to increase, albeit more quickly. The significant increase in δ appears as debonding occurs. A dimensionless parameter D is introduced to describe the damage level (Eq. (5)) [24], and $D = 0$ implies no damage, while $D = 1$ implies complete debonding. The shaded area under the $\delta - t$ curve in Fig. 3 represents the total interfacial energy J .

$$\mathbf{t} = \begin{Bmatrix} t_n \\ t_s \end{Bmatrix} = \begin{bmatrix} K_{nn} & K_{ns} \\ K_{sn} & K_{ss} \end{bmatrix} \begin{Bmatrix} \delta_n \\ \delta_s \end{Bmatrix} = \mathbf{K}\delta \quad (4)$$

$$D = \frac{\delta^f(\delta - \delta^0)}{\delta(\delta^f - \delta^0)}. \quad (5)$$

We used an interfacial stiffness $K_{nn} = K_{ss} = 1 \times 10^8$ GPa/m [6] for both normal and shear directions, and assumed no coupling between the two directions ($K_{ns} = K_{sn} = 0$ in Eq. (4)). The interfacial energy



(J) was set to 100 J/m^2 [26]. For the strong interface case, fibers surfaces were tied to the matrix, and the cohesive interface was not used, ensuring debonding did not occur. For the weak interface models, the cohesive interface was implemented, with an interface strength of $t_n^0 = t_s^0 = 30 \text{ MPa}$, which is 70% less than the matrix compressive strength (115 MPa). The weak interface can be regarded as a degraded interface, such as often results from ageing. The magnitude of glass fiber–epoxy interface strength was reported to be 10–100 MPa [27-30].

Post-debonding contact between fiber and matrix was enabled using “hard contact” in the normal direction and frictionless contact in the shear direction [24]. “Hard contact” behavior can be described by Eq. 6:

$$\begin{cases} p=0 & \text{for } h < 0 \text{ (open), and} \\ h=0 & \text{for } p > 0 \text{ (closed)} \end{cases}, \quad (6)$$

in which p is the contact pressure between two surfaces, and h is the “overclosure” (the interpenetration of the surfaces). Thus, for “hard contact,” extrusion of the two surfaces into each other is forbidden, and contact stress can only be compressive. The frictionless assumption in the shear direction can lead to some underestimation of overall stiffness and strength, and there is no reliable measured data of the interface friction that can be used in the model. The cohesive debonding rule and post-cracking contact of the interface were implemented using contact definition module in Abaqus.

4. Failure Plane Orientation Prediction

As mentioned, failure plane angle of UD composites under transverse compression is generally greater than that of neat matrix, although they are both in the range of 50° – 60° . The difference can

“Transverse compression failure of unidirectional composites” Y. Hu, N. Kar, and S. Nutt, Polymer Compos. (2014) DOI<<http://dx.doi.org/2010.1002/pc.22996>>



be explained by the distortion of the matrix shear band caused by the presence of fibers. As f increases, the fiber distribution approaches hexagonal packing, which is the densest possible arrangement. Figure 4 shows a cross-section of a UD composite with regular hexagonal packing of fibers, in which both the fiber diameters (d) and the distance between adjacent fibers (D) are uniform.

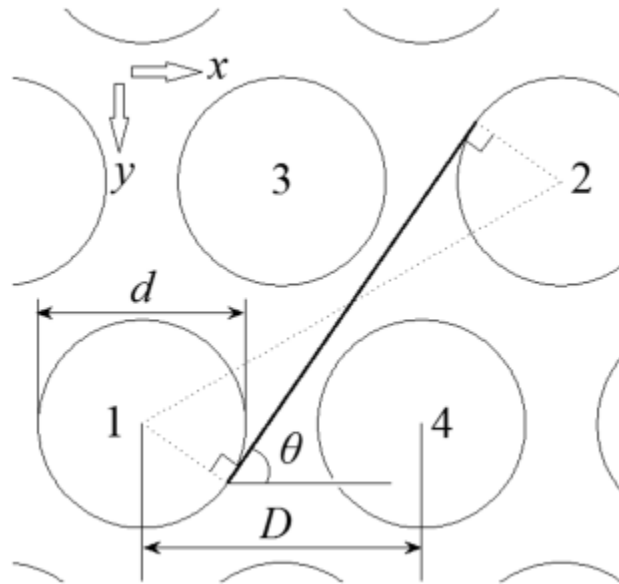


Figure 4. Plastic shear band in hexagonal model.

A dimensionless parameter $\zeta = d/D$ is used to describe the areal density of fibers: $\zeta = 0$ indicates a neat matrix condition, while $\zeta = 1$ indicates the maximum theoretical fiber volume fraction. The relationship between ζ and the fiber volume fraction (f) can be derived from the geometric relationship as (Eq. 7):

$$f = \frac{\pi}{2\sqrt{3}} \zeta^2, \quad (7)$$

in which $f_{\max} = \frac{\pi}{2\sqrt{3}} \approx 91\%$ when $\zeta = 1$.



As shown in Fig. 4, when this model undergoes compression in the y direction (the x direction is assumed to be unconstrained), the matrix shear stress reaches a maximum and forms a shear band along the bold line [4], which is the common tangent of fibers #1 and #2. This plastic shear band can be the most likely potential failure plane, and the angle θ can be calculated as (Eq. (8)):

$$\begin{aligned}\theta &= \frac{\pi}{6} + \sin^{-1}\left(\frac{d/2}{\sqrt{3}D/2}\right) = \frac{\pi}{6} + \sin^{-1}\left(\frac{\xi}{\sqrt{3}}\right) \\ &= \frac{\pi}{6} + \sin^{-1}\left(\sqrt{\frac{2}{\sqrt{3}\pi}f}\right).\end{aligned}\tag{8}$$

However, Eq. (8) is not sufficient to limit the entire range of θ , because other factors become critical when f approaches minimum and maximum. The lower bound of θ is restrained by the neat matrix failure angle θ_{matrix} when f approaches 0 and the fibers are sparse and cannot effectively deflect the shear band. The higher bound of θ is restrained by the hexagonal packing of fibers. When f approaches a critical value and the shear band trace contacts fibers #3 and #4 in Fig. 4, the shear band is locked at 60° by the surrounding fibers. This critical f is 68%, back-calculated from Eq. (8). Applying these two constraints, the final form of the $f-\theta$ relation is (Eq. (9)):

$$\theta = \begin{cases} \theta_{\text{matrix}} & \text{for } f \rightarrow 0 \\ 30^\circ + \sin^{-1}(0.61\sqrt{f}) & \text{for } f \leq 68\% \\ 60^\circ & \text{for } f \geq 68\% \end{cases}\tag{9}$$

However, the above relation is based on regular hexagonal packing of fibers, although in practice, fiber distributions in composites are random. Thus, experiments and simulations of samples with randomly distributed fibers are required to validate this prediction, as described below. Note that the higher bound of 60° predicted by Eq. (9) is consistent with Christensen's continuum-based



theory [11], implying a possible intrinsic connection between the micro-level and macro-level models.

5. Results and Discussion

5.1 Model Size Validation

The size of the finite element model and the number of fibers included in the model may significantly influence the results. Thus, different model sizes were studied, and the results were compared to ensure that the model size was sufficiently large to achieve stability and to produce a statistical average of results. The control model size was $(100 \times 100) \mu\text{m}$, as previously discussed. One control model with $f = 50\%$ was selected to compare with a model twice as large $(141 \times 141) \mu\text{m}$ with the same fiber loading. The number of fibers was 65 in the control model and 130 in the large model. Both models used the same generation algorithm to achieve randomly distributed fibers. The stress–strain curves of the two models are compared in Fig. 5.

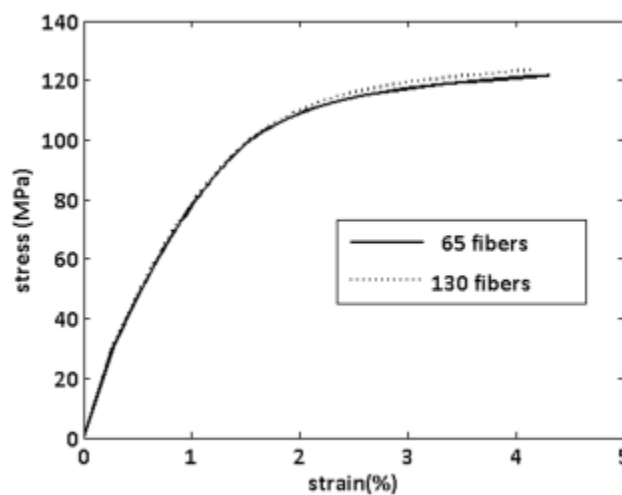


Figure 5. Model size sensitivity.



As shown in Fig. 5, the two curves overlap in the elastic range, and the maximum difference in the plastic range is less than 2%. Considering the difference in fiber distributions, the 2% difference is acceptable, and the model size of $(100 \times 100) \mu\text{m}$ is appropriate for current problem. All finite element results below are from $(100 \times 100) \mu\text{m}$ models.

5.2 Stress-Strain Curves

Figure 6 shows the stress–strain curves of models and experiment. Each curve represents the average of all the models/samples at the same fiber volume fraction level. The “+” mark on the experimental curve indicates the point of brittle fracture, which occurs at a failure strain $<2\%$. The standard deviation is less than 4% for both experiment and simulation curves. Note that the experimental curve may not be comparable with simulated curves because (1) the experimental curve is for a sample with $f=70\%$, while the simulated curves are for models with $f=10\text{--}50\%$, and (2) the mechanical properties input of the fiber, matrix, and interface in the models are from literature data and not from measured values.

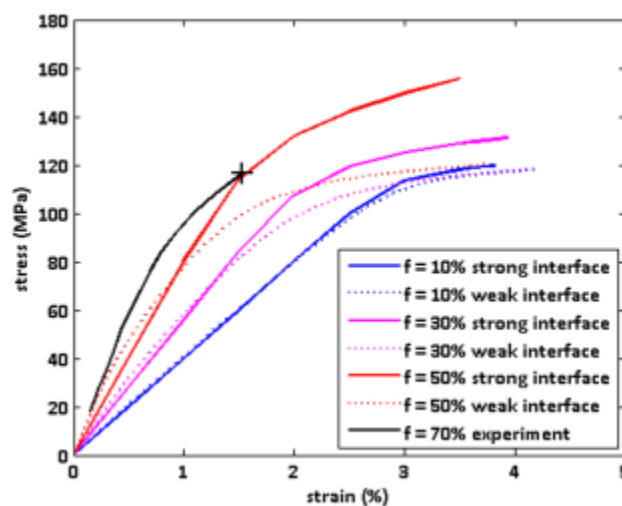


Figure 6. Stress–strain curves of finite element models.



From Fig. 6, modulus in transverse direction increases with f as predicted by a simple rule-of-mixtures (Eq. (10)).

$$\frac{1}{E_c} = \frac{f}{E_f} + \frac{1-f}{E_m}, \quad (10)$$

in which E_c , E_f , and E_m are the modulus of the composites, fiber, and matrix, respectively. For $f=10\%$, no difference was observed between strong and weak interfaces, because fibers are sparse and have negligible effect on the overall behavior. For $f=30\%$ and 50% , yielding of the weak-interface models occurs earlier than the strong-interface models. This is caused by interfacial debonding before matrix yield, as the interface strength is 70% less than the matrix yield strength.

For all weak-interface models in Fig. 6, the maximum stress that can be reached is ~ 115 MPa, the matrix compressive yield strength. Thus, when the interface strength is significantly less than the strength of the matrix and when massive interface failure occurs before matrix yield, the strength of the composites is determined by the matrix, regardless of the fiber content. For the strong-interface models in Fig. 6, strength increases with f , a result of the deviatoric stress level change with f [2, 22]. As reported previously [2, 22], when the fiber volume fraction increases, under external transverse compression load, the stress state in the matrix tends to be tri-axial instead of uniaxial. Thus, the deviatoric stress (shear stress) in the matrix decreases as f increases, and leads to a higher compressive strength because matrix failure is triggered by shear failure along plastic shear bands.

Figure 7 shows the von Mises stress for the two $f=30\%$ and $f=50\%$ strong-interface models under the load of 100 MPa. Here, the von Mises stress was used as an indication of deviatoric stress level. The high-stress regions (>90 MPa) constitute greater areas in the $f=30\%$ model (36% of total matrix area) than in the $f=50\%$ model (22% of total matrix area). Thus, the $f=30\%$ model will fail earlier



than the $f=50\%$ model. In comparison, Fig. 8 shows the von Mises stress for the same models under the same load when a weak interface was assumed. In this case, the high-stress regions of the two models are similar (30% of total matrix area), and they show similar compressive strength values in Fig. 6. Comparing Figs. 7 and 8, the stress concentration in the matrix was relieved in weak-interface models. Interface debonding diminished the load transfer between fiber and matrix, and the influence of fibers on matrix was reduced. Thus, the stress was more evenly distributed in the matrix, and the matrix behaved more like a neat resin.

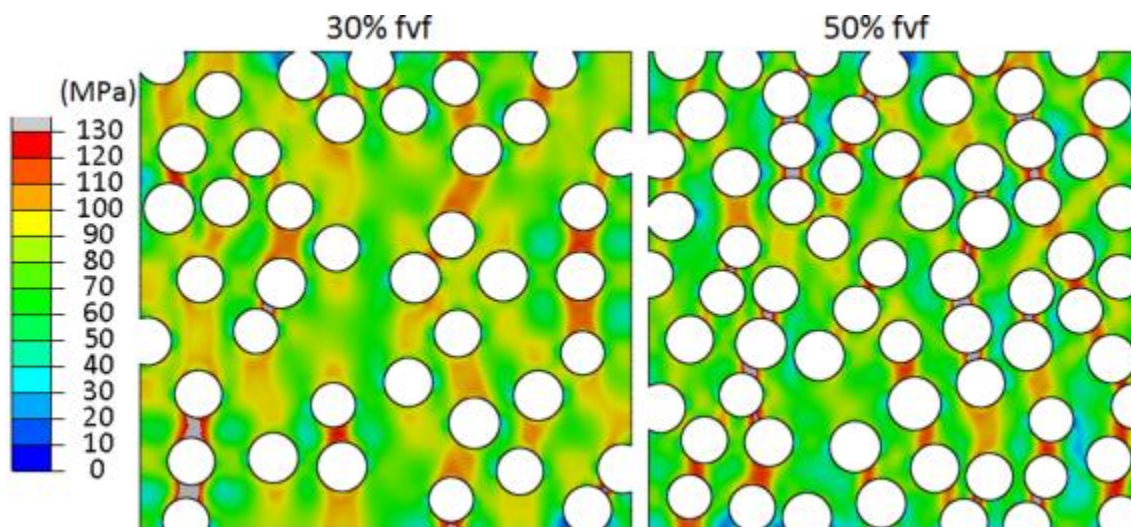


Figure 7. von Mises stress for strong interface models.

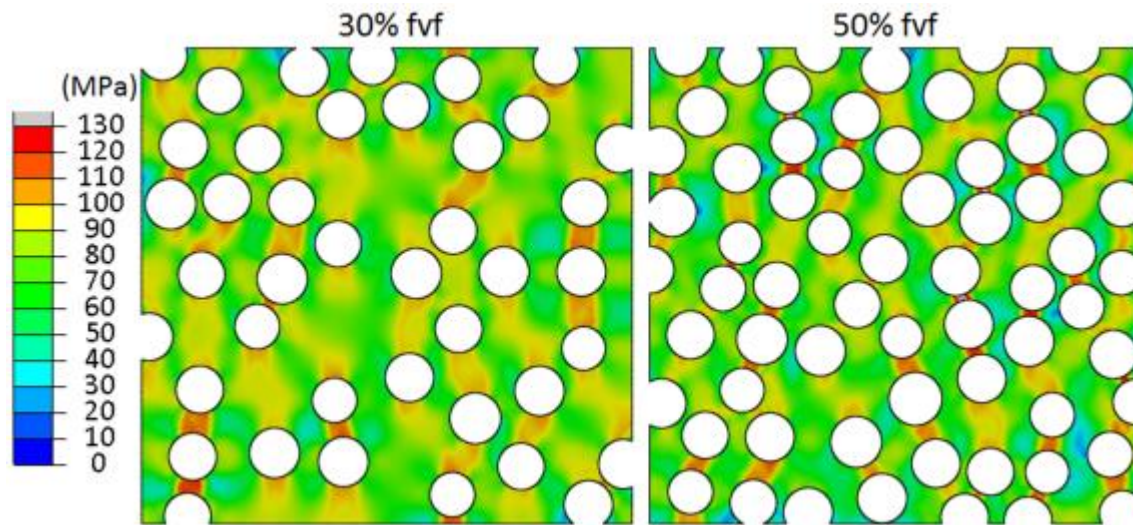


Figure 8. von Mises stress for weak interface models

Figure 9 shows the strain concentration effect in an $f = 50\%$ strong-interface model. The solid line indicates the overall compressive strain in the composite, while dotted line indicates the matrix strain at its maximum location in the model. From Fig. 9, when the matrix strain reaches 30% and shows severe plasticity, the overall strain in the model is only 3% and shows slight plasticity. Thus, the maximum strain magnification factor in the matrix is up to $10\times$ in the plastic region. Although the matrix can be ductile, the composite may exhibit brittle failure, especially when the fiber volume fraction is high. This simulation result is consistent with previous reports [2-6], in which most composites showed brittle fracture in transverse loading. The strain concentration effect is a result of the large modulus difference between fiber (72.3 GPa) and matrix (3.1 GPa). In composites with intact interfaces, the stress is continuous through the fiber–matrix interface. Because of the modulus mismatch, the strain is discontinuous and shows an abrupt change at the interface. When the fiber–matrix bonding is weakened (Fig. 8), the stress through the interface is no longer continuous, and as a result, matrix strain concentration is reduced.

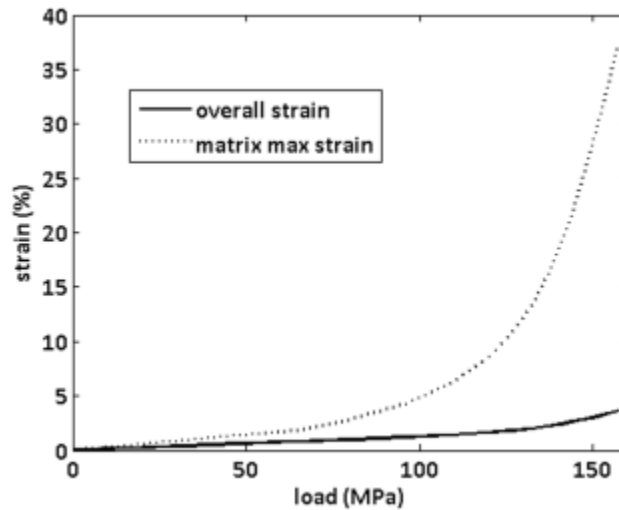


Figure 9. Strain concentration in matrix at $f = 50\%$.

5.3 Failure Plane Orientation

Figure 10 shows the measured crack angles for one cuboidal sample at the same location at different magnifications. The crack angle is consistent from the millimeter scale to the micrometer scale. The rightmost image in Fig. 10 is the same scale as the RVE models. Thus, the failure plane angles from experiment and simulation are comparable in length scale. The average crack angle from 16 samples was 60° with a standard deviation of 5%. This crack angle at $f = 70\%$ is consistent with reported values [5] and with Eq. (9) prediction. The image of the fracture surface is inset in the leftmost figure. Both bare glass fiber surface and matrix fracture are shown, indicating a combined failure of matrix and interface. Whether the damage is initiated/dominated by matrix shear or interface debonding is difficult to determine from the images.

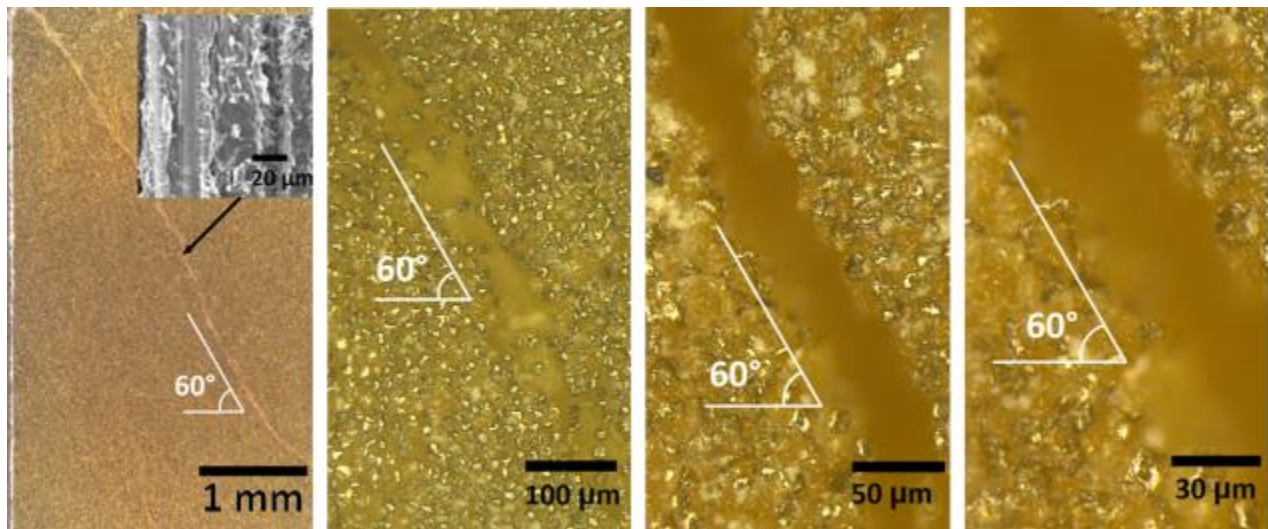


Figure 10. Experimental crack angle and fracture surface.

Figure 11 shows the simulated plastic strain contours for different fiber volume fractions and different interface conditions. These contours were generated in the plastic range of the models shown in Fig. 6. Figure 11 a and b feature the same $f=10\%$ model, while Fig 11c and d are from the same $f=30\%$ model, and Fig. 11e and f are from the same $f=50\%$ model. A strong interface was used in Fig. 11a, c, and e, while a weak interface was used in Fig. 11b, d, and f. Each model at a specific fiber volume fraction level represents only 1 of the 10 iterations, each with different fiber distributions. Figure 11c, d, e, and f are identical to the models in Figs. 7 and 8. For $f=10\%$ (Fig. 11a and 11b), plastic shear bands form around fibers. Small strain concentrations appear in regions near the interface. Multiple shear bands form in the matrix, and they all show an angle of 52° , which is identical to the neat matrix failure angle predicted by Eq. (2). No difference is observed for strong and weak interfaces. Thus, at $f=10\%$, the fiber content is so low that it has a negligible effect on the composite mechanical behavior, and the composite behavior is similar to the neat resin. In contrast, for $f=30\%$ and 50% models, shear bands are random and their orientations are much influenced by the packing of fibers.

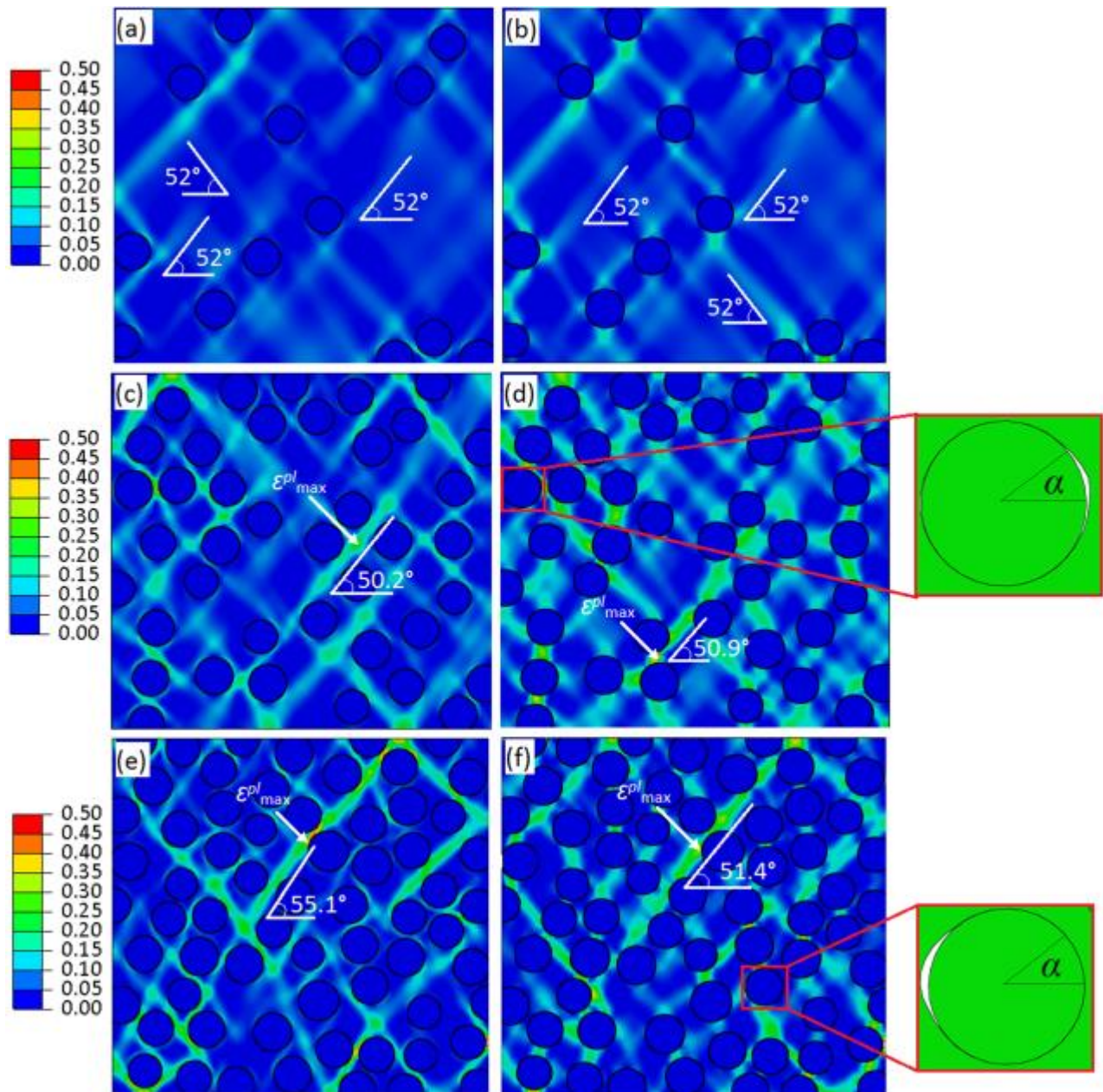


Figure 11. Simulated plastic shear bands.

To determine the failure plane for these models, the location of the maximum plastic strain ($\epsilon_{pl_{max}}$) is marked in each figure, and the shear band showing the maximum plastic strain in the model is regarded as the potential failure plane. The angle of this plane was measured as the angle of the centerline of the shear band, as shear bands generally have widths equal to the spacing between neighboring fibers. In this way, the failure plane for a single model was determined. However, the



failure plane angle θ showed slight but consistent variance from different models because the arrangement of fibers for each model was random. The value of θ from the 10 iterations of the models at each fiber volume fraction level was summarized to yield a valid statistical result and to minimize the artificial measurement error. The standard deviation was less than 6% for each fiber volume fraction level. (This issue is addressed later.) Note that the angles marked in Fig. 11c–f are only for these specific models and do not represent the average from 10 iterations. For Fig. 11d and f, one fiber was magnified to show the interface debonding state. The polar coordinate α was constructed regarding $\alpha = 0$ at the horizontal position.

Figure 12 plots the normal (δ_n) and shear (δ_s) debonding around these two fibers in Fig. 11d and f along the circumferential direction. From Eq. (5), a debonding displacement of $\delta = 0.015 \mu\text{m}$ leads to a damage degree of $D = 99\%$. Thus, shear debonding is the dominant debonding mode for both models and occurs at nearly 100% of interface area. In comparison, normal debonding occurs only at 30% of interface area and only at $\alpha = 0$ and $\alpha = 180^\circ$. This debonding pattern is typical under uniaxial compression: separation occurs at horizontal sites while the top and bottom of the fiber are in compression. The magnitudes of normal and shear separation are similar.

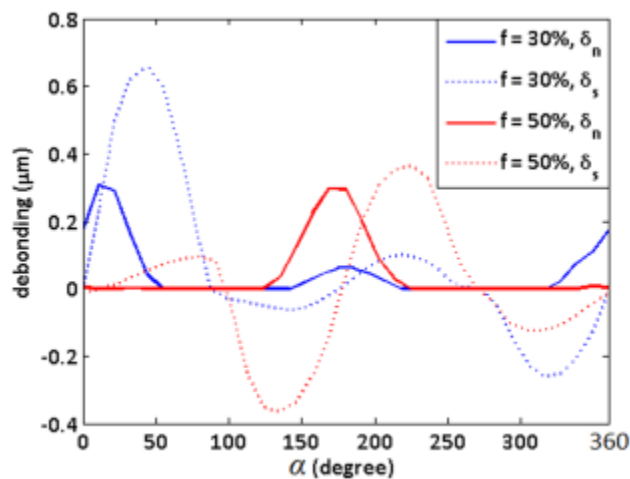


Figure 12. Debonding around fiber's circumference.



The deviation effect of fibers on matrix shear band is clearly illustrated in Fig. 11, which confirms the assumption in Failure Plane Orientation Prediction section. As fibers become more densely packed, the arrangement gradually shifts from random packing to hexagonal packing, as hexagonal packing is the most efficient arrangement. Thus, the hexagonal model in Failure Plane Orientation Prediction section is more applicable to high fiber loading cases. Shear bands in strong-interface models are continuous and smooth, while the shear bands in weak-interface models are disconnected and random. This phenomenon is caused by the state of the interface: for the intact interface model, the stress field is continuous everywhere in the model, while for the damaged interface model, the stress is discontinuous across the interface, causing the discrete appearance of the strain field. Thus, the influence of fibers on matrix is diminished in damaged interface models, and their failure plane angles deviate from the prediction in Failure Plane Orientation Prediction section, as interface debonding is not accounted for in the hexagonal model.

In Fig. 13, we sum the θ versus f data taken from experiments, from measured values in the literature [2, 5-7], and from simulations in this work. Each simulation data point represents the average of the 10 iterations of models, and the standard deviation is less than 6% for all simulated failure plane angles. The approach for determining the angle is consistent, as described previously (see Fig. 11). In the low range of f , experimental data are not available, as $f > 50\%$ for most composites. Both strong- and weak-interface models at $f = 10\%$ show $\theta = 52^\circ$, and this value is the same as the input neat matrix failure plane angle, confirming the negligible role of fibers in the transverse direction. In the medium range of f , reported θ values [2, 6] and models with strong interface agree with the hexagonal model prediction, while weak-interface models show failure plane angles of $\sim 52^\circ$ at all fiber volume fraction levels. Therefore, Eq. (9) is applicable when matrix



yield dominates the failure. In the high range of f , simulation data are not available because of the numerical convergence difficulty in the fiber loading model. All measured and reported values [5] are 60° , in accordance with the prediction of Eq. (9). Whether the failure is interface-dominated or not is unclear for these data points.

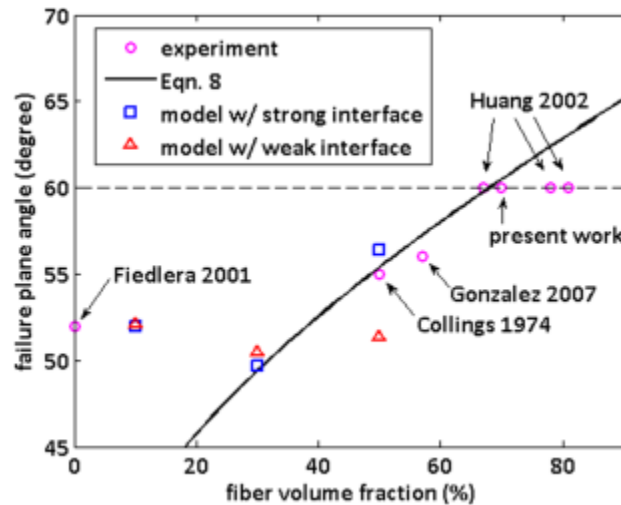


Figure 13. Failure plane angle versus fiber volume fraction.

6. Conclusions

The effects of fiber volume fraction and interface strength on the uniaxial transverse compressive behavior of UD composites were studied through experimental measurements and finite element simulations. A model featuring hexagonal packing of fibers was proposed to predict the failure plane angle of composites. Predictions were consistent with published data for composites with $f > 50\%$ (data for composites with $f < 50\%$ are not available). The predicted failure plane angle for $f > 68\%$ was fixed at 60° , although this prediction awaits validation by direct observation and simulation. The model predictions also were consistent with finite element analyses assuming strong interfaces,



although the predictions were not consistent with weak-interface finite element models because debonding was not taken into account.

Analysis of stress–strain curves shows that composites become more brittle as the fiber volume fraction increases, a consequence of strain concentration. Although the neat resin can be ductile, the failure of composites is generally brittle because the strain magnification factor in the matrix can be up to 10× in the plastic range. The compressive strength values determined from finite element simulations indicate a strength increase with increasing fiber loading for strong-interface models. The mechanism responsible for this phenomenon is the deviatoric stress decrease with increasing fiber loading (provided the interface is intact). However, for the weak interface condition, interfacial debonding occurs prior to matrix yield, leading to behavior similar to the unreinforced matrix, regardless of fiber volume fraction.

Insights into the micromechanical effects of fibers and interfaces are critical to understanding deformation and failure mechanisms in UD composites. Using the methods presented here, crack angle and strength can be estimated before testing, and the failure criteria can be used to guide design. The failure plane angle range and failure modes from our investigations are consistent with those of Christensen's continuum-based theory: failure is ductile and the failure plane angle is low at low fiber volume fractions, while failure is brittle and the failure plane angle is high at high fiber volume fractions. This consistency suggests a possibility of linking the two scales to build accurate multi-scale failure models.

Acknowledgements: Composite Technology Corporation (CTC, Irvine, CA) is gratefully acknowledged for the supply of samples.

References:

“Transverse compression failure of unidirectional composites” Y. Hu, N. Kar, and S. Nutt, *Polymer Compos.* (2014) DOI<<http://dx.doi.org/2010.1002/pc.22996>>



1. N.K. Kar, Y. Hu, E. Barjasteh, and S.R. Nutt, *Composites: Part B*, 43, 2115 (2012).
2. T.A. Collings, *Composites*, 5, 108 (1974).
3. I.M. Daniel, J. Luo, P.M. Schubel, and B.T. Werner, *Compos. Sci. Technol.*, 69, 764 (2009).
4. S.Y. Hsu, T.J. Vogler, and S. Kyriakides, *Int. J. Plast.*, 15, 807 (1999).
5. Y.K. Huang, P.H. Frings, and E. Hennes, *Composites: Part B*, 33, 109 (2002).
6. C. Gonzalez and J. LLorca, *Compos. Sci. Technol.* 67, 2795 (2007).
7. B. Fiedler, M. Hojo, S. Ochiai, K. Schulte, and M. Ando, *Compos. Sci. Technol.* 61, 1615 (2001).
8. R. Quinson, J. Perez, M. Rink, and A. Pavan, *J. Mater. Sci.*, 32, 1371 (1997).
9. A.F. Yee, J. Du, and M.D. Thouless, *Polym. Blends* (2000).
10. B. Paul, *J. Appl. Mech.*, 06, 259 (1961).
11. R.M. Christensen and S.J. DeTeresa, *Int. J. Solids Struct.*, 40, 7055 (2003).
12. A. Puck and H. Schurmann, *Compos. Sci. Technol.*, 58, 1045 (1998).
13. Z. Hashin, *J. Appl. Mech.*, 47, 329 (1980).
14. S.W. Tsai and E.M. Wu, *J. Compos. Mater.*, 5, 58 (1971).
15. S.T. Pinho, C.G. Dávila, P.P. Camanho, L. Iannucci, and P. Robinson, NASA/TM-2005-213530.
16. S. Blassiau, A. Thionnet, and A.R. Bunsell, *Compos. Struct.*, 74, 303 (2006).
17. E. Correa, V. Mantic, and F. Paris, *Eng. Fract. Mech.*, 75, 4085 (2008).
19. L.P. Canal, J. Segurado, and J. LLorca, *Int. J. Solids Struct.*, 46, 2265 (2009).
20. E. Totry, C. Gonzalez, and J. LLorca, *Compos. Sci. Technol.*, 68, 829 (2008).
21. E. Ghassemieh and V. Nassehi, *Polym. Compos.*, 22, 542 (2001).
22. J.M.M. Kok and H.E.H. Meijer, *Composites: Part A*, 30, 905 (1999).
23. J. Segurado and J. LLorca, *J. Mech. Phys. Solids*, 50, 2107 (2002).

“Transverse compression failure of unidirectional composites” Y. Hu, N. Kar, and S. Nutt, *Polymer Compos.* (2014) DOI<<http://dx.doi.org/10.1002/pc.22996>>



24. Abaqus user manual, v6.11, Dassault Systemes (2011).
25. Ph. Menétrey and K.J. Willam, *ACI Struct. J.*, 92, 311 (1995).
26. X.F. Zhou, H.D. Wagner, and S.R. Nutt, *Composites: Part A*, 32, 1543 (2001).
27. J.L. Koenig and H. Emadipour, *Polym. Compos.*, 6, 142 (1985).
28. Y.T. Liao, *Polym. Compos.*, 10, 424 (1989).
29. V. Rao and L.T. Drzal, *Polym. Compos.* 12, 48 (1991).
30. J.P. Favre, M.H. Auvray, P. Cheneau-Henry, C. Galiotis, C. Vlattas, A. Paipetis, M. Pegoraro, F. Severini, L. Di Landro, and L. Yuan, *Polym. Compos.* 17, 937 (1996).